Tailoring Dirac Fermions by *In-Situ* Tunable High-Order Moiré Pattern in Graphene-Monolayer Xenon Heterostructure

Chunlong Wu,[1,*] Qiang Wan,[1,*] Cao Peng,[1] Shangkun Mo,[1] Renzhe Li,[1] Keming Zhao,[1] Yanping Guo,[2]
Shengjun Yuan[2], Fengcheng Wu[2,3,†] Chendong Zhang,[2,3] and Nan Xu[1,3,‡]

[1]*Institute for Advanced Studies, Wuhan University, Wuhan 430072, China*
[2]*School of Physics and Technology, Wuhan University, Wuhan 430072, China*
[3]*Wuhan Institute of Quantum Technology, Wuhan 430206, China*

We report an experimental study of a high-order moiré pattern formed in graphene-monolayer xenon heterostructure. The moiré period is *in situ* tuned from few nanometers to $+\infty$, by adjusting the lattice constant of the xenon monolayer through annealing. Using angle-resolved photoemission spectroscopy, we observe that Dirac node replicas move closer and finally overlap with a gap opening, as the moiré pattern expands to $+\infty$ and evolves into a Kekulé distortion. A moiré Hamiltonian coupling Dirac fermions from different valleys explains experimental results and indicates narrow moiré band. Our Letter demonstrates a platform to study continuous evolution of the moiré pattern, and provides an unprecedented approach for tailoring Dirac fermions with tunable intervalley coupling.

DOI: 10.1103/PhysRevLett.129.176402

Moiré superlattices provide a promising playground for explorations of novel quantum phases and phase transitions. In twisted bilayer graphene (tBLG), the moiré pattern couples Dirac fermions from the same valley but different layers [Fig. 1(a)], and results in moiré bands with extremely narrow bandwidth at the magic-angle condition [1]. Novel quantum phases, including correlated insulators [2–5], superconductivity [6–13], magnetism [14–17], and non-trivial topological states [18–20], are experimentally realized by designing moiré patterns and tuning the electron filling of moiré bands. The flat moiré bands in tBLG are directly observed by state-of-the-art angle-resolved photoemission spectroscopy (ARPES) with nanoscale real-space resolution [21,22]. Similarly, a moiré pattern in twisted bilayer transition metal dichalcogenides also induces flat moiré bands [23] and novel quantum states [24–26] like Mott insulators [27] and the generalized Wigner crystal phase [28].

These novel quantum phenomena are very sensitive to the lattice structures of moiré patterns. Therefore, *in situ* tunable moiré patterns can provide a powerful tool to design electronic structures and quantum phases. The moiré pattern is determined by twist angle (θ) and lattice constant mismatch ($\Delta a = a_1 - a_2$) between the constituent layers. One way of tuning a moiré pattern is to control the twist angle θ. Using an atomic force microscope tip to push the specially shaped BN on graphene, θ can be changed *in situ* [29,30].

In this Letter, we report a new route to realize *in situ* tunable high-order moiré patterns. It is realized in graphene-monolayer xenon heterostructures, which we term as G/mXe, with moiré period tuned in a range from nanometer scale to $+\infty$. Distinct from the previous method by changing θ, we tune the lattice constant of the Xe monolayer by an annealing process, therewith to control the mismatch Δa term. Using ARPES, we directly observe the replicas of graphene Dirac cones generated by the moiré pattern, which move close to each other in momentum space (k space) as the moiré pattern expands in real space. The replicas finally overlap with each other as the moiré period approaches $+\infty$ and the moiré pattern evolves into a commensurate structure where a $\sqrt{3} \times \sqrt{3}$ superlattice with
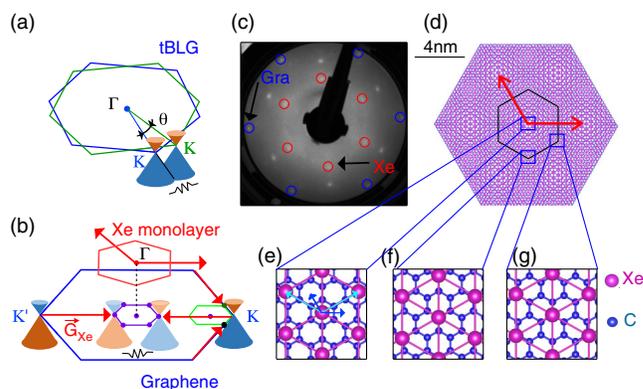
FIG. 1.   (a) Schematic first-order moiré effect in tBLG systems in k space. (b) Schematic high-order moiré effect in G/mXe. (c) LEED pattern of moiré pattern measured at $T = 60$ K. (d) Large-scale atom arrangements showing moiré pattern of G/mXe in real space. (e)–(g) Atom arrangements in zoomed-in areas at the center and neighboring corners of the moiré pattern, respectively. The primitive vectors of graphene and Xe monolayer are labeled in (e).

Kekulé distortion develops in graphene. A gap with $\Delta_{\text{Kekulé}} \sim 0.4$ eV is then observed at the Dirac point, induced by intervalley coupling of Dirac fermions. A continuum moiré Hamiltonian $\mathcal{H}$ of G/mXe explains the experimental results, and indicates moiré flatbands for large moiré periods. Interestingly, $\mathcal{H}$ in G/mXe couples Dirac fermions from different valleys [Fig. 1(b)], in contrast to that in tBLG coupling Dirac fermions from different graphene layers [Fig. 1(a)]. Our Letter not only offers a promising platform for tailoring Dirac fermions with tunable intervalley coupling, but also provides a novel way to induce and tune the moiré pattern in 2D materials by noble gas monolayer.

Monolayer graphene was achieved by the high-temperature annealing process [31] of n-type 6H SiC(0001) from PrMat. The monolayer graphene samples were characterized by scanning tunneling microscopy measurements. Xe monolayers were formed on a clean graphene surface by depositing slightly thicker layers at $T = 44$ K with Xe pressure of 1×10^{-9} Torr and then annealing at a temperature above the second-layer desorption temperature (T_s). ARPES measurements were performed at the home-designed facility with photon energy $h\nu = 21.2$ eV and spot size about 0.5 mm. Low-energy electron diffraction (LEED) patterns were measured on the same sample surface using electron energy of 105 eV, with a facility mounted on the ARPES chamber.

The Xe monolayer has been grown on a graphite surface in Ref. [32], forming a hexagonal structure with primitive vectors 30° rotated from those of graphite. Our LEED patterns [Fig. 1(c)] and ARPES results consistently indicate the same structure in G/mXe [Figs. 1(d)–1(g)]. Both $\Delta a = a_{\text{Xe}} - a_{\text{Gra}}$ and θ between the unit cells of graphene and Xe monolayer are large [Fig. 1(e)], where $\theta = 30°$, $a_{\text{Gra}} \approx 2.46$ Å and $a_{\text{Xe}} \sim 4.4$ Å are the lattice constants of graphene and Xe monolayer, respectively (a_{Xe} depends on the annealing process as discussed in the following). Therefore, the first-order moiré effect directly related to Δa and θ is expected to be weak in G/mXe. However, a $\sqrt{3} \times \sqrt{3}$ supercell of graphene and the unit cell of Xe are rotationally aligned ($\theta' = \theta - 30° = 0°$) and have a small lattice constant mismatch $\Delta a' = a_{\text{Xe}} - \sqrt{3}a_{\text{Gra}}$ [Fig. 1(e)]. Therefore, the high-order moiré effect arising from θ' and $\Delta a'$ is expected to be pronounced with moiré period a'_m given by

$$a'_m = \frac{a_{\text{Xe}} a_{\text{Gra}}}{\Delta a'}, \qquad (1)$$

The large-scale atomic arrangement plotted in Fig. 1(d) confirms the high-order moiré pattern in G/mXe. Similar to tBLG, the moiré pattern in G/mXe forms a hexagonal structure, with center and corner regions showing different stacking forms [Figs. 1(e)–1(g)].

In k space, the moiré pattern modulates electronic structure. Dirac cone replicas are induced by shifting the original Dirac cones of graphene with momentum transfers
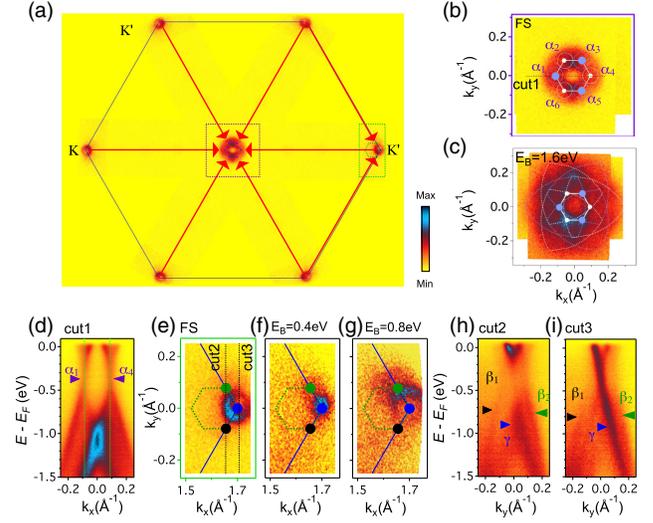
FIG. 2. (a) Fermi surface mapping of G/mXe. (b),(c) Constant energy intensity plots near the Γ point at E_F and $E_B = 1.6$ eV, respectively. (d) The band structure along the cut1 in (b). (e)–(g) Evolution of constant energy intensity plots near the K point. (h),(i) Photoemission intensity plots along cut2 and cut3 labeled in (e), respectively.

of the first-shell reciprocal lattice vectors of Xe monolayer $\vec{G}_{\text{Xe}}$. As illustrated in Fig. 1(b), replicas are located at the corners of a hexagon centered at the Γ point. This hexagon is the moiré Brillouin zone (BZ) corresponding to the high-order moiré period a'_m (Fig. S1 in the Supplemental Material [33]). In addition, replicas can be induced near the $K(K')$ point also by scatterings of momentum $\vec{G}_{\text{Xe}}$. Two replicas and one original Dirac cone sit at three corners of a hexagon that is centered at the $\vec{G}_{\text{Xe}}$ point. This hexagon is a momentum-shifted copy of the moiré BZ centered at the Γ point. The replicas have the same valley arrangement as the original Dirac cones of graphene, i.e., the nearest neighbor Dirac cones have different chirality.

We perform ARPES measurements on G/mXe at $T = 67$ K and directly observe the Dirac replicas [Fig. 2(a)], together with dispersive bands of Xe monolayer at higher binding energy (E_B) (Fig. S2 in the Supplemental Material [33]). As shown in Figs. 2(b)–2(c), the spectra near the Γ point is fully consistent with six replicas α_1-α_6 sitting at corners of the moiré BZ. Figure 2(d) displays the band structure along cut 1 in Fig. 2(b), with replicas α_1 and α_4 clearly observed; we determine the momentum center of the α_4 replica to be $\kappa = (0.09 \text{ Å}, 0)$ at $T = 67$ K. We also clearly resolve the replicas β_1 and β_2 in the constant E_B plots [Figs. 2(e)–2(g)] and band structure [Figs. 2(h)–2(i)] near the K point, in addition to the original Dirac cone γ.

We manage to continuously control a_{Xe} by annealing at different temperatures above the second-layer desorption temperature T_s and therewith to tune $a_{m'}$ in G/mXe with $\Delta a'$ term in Eq. (1). The tunable moiré pattern is demonstrated by the moving of replicas in k space as a function of
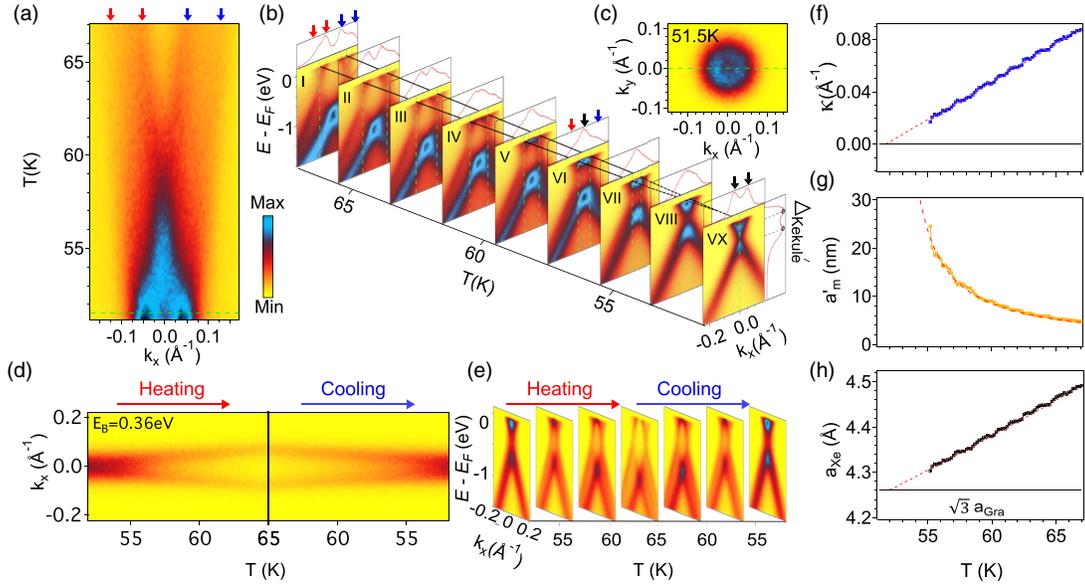
FIG. 3. (a) T-dependent photoemission data at E_F along the Γ-K direction. (b) Corresponding T-dependent band structure. The momentum distribution curves (MDCs) at E_F are also plotted on the top. The red and blue arrows indicate the Fermi momenta of the α_1 and α_4 replicas, respectively. (c) The FS mapping near the Γ point at $T = 51.5$ K. (d) Photoemission data at $E_B = 0.36$ eV along the Γ-K direction with both increasing and decreasing temperature. (e) Corresponding temperature evolution of band structure near the Γ point. (f)–(h) T-dependent data of κ, a'_m and a_{Xe}, respectively. The dashed lines are fitting curves. The value of $\sqrt{3}a_{Gra}$ is indicated by the solid line in (h).

temperature shown in Figs. 3(a) and 3(b). As T decreases, the α_1 and α_4 replicas move close to each other, touch at E_F at $T = 57.5$ K [Fig. 3(b-VI)] and finally overlap at $T \sim$ 51.5 K [Fig. 3(b-VX)]. Here the Fermi energy E_F is 390 meV above the Dirac points. The FS also evolves from six pockets at $T = 67$ K [Fig. 2(d)] into a single pocket at $T = 51.5$ K [Fig. 3(c)]. Such evolution of a moiré pattern is reversible with both increasing and decreasing temperature [Figs. 3(d) and 3(e)]. Note that the change in a_{Gra} is negligible in the temperature range of $50 \sim 70$ K. Therefore, the tunable moiré pattern is induced by variation of the lattice constant of the Xe monolayer a_{Xe}. The changes in a_{Xe} are directly shown in temperature dependent LEED measurments, which are also reversible with temperature cycling (Fig. S3 in Supplemental Material [33]).

We can determine the T dependence of the replica's momentum κ, and extract a'_m and a_{Xe}, with the results shown in Figs. 3(f)–3(h), respectively. The magnitude $|\kappa|$ has a good T-linear dependence [Figs. 3(a), 3(b), and 3(f)]. Results in Fig. 3(h) indicate that ARPES is a sensitive method to determine lattice constant of Xe monolayer in G/mXe with the resolution of the order of 0.1 Å.

As a_{Xe} approaches $\sqrt{3}a_{Gra}$ at low T, a'_m diverges in G/mXe. In this process, the high-order moiré pattern with $a'_m \to +\infty$ evolves into a Kekulé distortion with a $\sqrt{3} \times \sqrt{3}$ reconstruction of graphene [38]. Replicas near the Γ point overlap with each other with $\kappa \to 0$. Because the nearest replicas have different valley chirality, the Kekulé gap Δ is opened by intervalley coupling. The energy

distribution curve (EDC) at the Γ point for $a'_m \to +\infty$ shows a double-peak line shape with an energy separation around 0.4 eV [Fig. 3(b-VX)], where the line shape is similar to that in other graphene systems [39] with a Kekulé gap. The observation of the Kekulé gap excludes the photoelectron surface diffraction as the reason of replicas in ARPES experiments.

The *in situ* tunable moiré pattern in G/mXe offers an opportunity to study the moiré modulation effect on Dirac fermions with variable a'_m. In Fig. 4(a), we plot the band structure of G/mXe near the K point with different a'_m, where the original Dirac cone γ remains at the K point. As shown in Fig. 4(b), the EDC at the K point for $a'_m = 5$ nm has a single peak feature, similar to EDC of pristine graphene. The additional spectra weight at $E_B > 1$ eV corresponds to β_2 replica in Fig. 4(a-I). For larger a'_m, $|\kappa|$ becomes smaller rapidly and the replicas β_1 and β_2 move close to the γ cone. The spectra weight corresponding to replicas shifts in energy towards the Dirac point, leading to a broad peak with nearly flat top for $a'_m = 10$ and 15 nm. As a'_m further increasing, the EDC evolves into a double-peak shape. An energy gap with $\Delta \sim 0.4$ eV is identified at the K point as a Kekulé distortion forms at $a'_m \to +\infty$, which is consistent with $\Delta_{Kekulé}$ observed at the Γ point.

To interpret the experimental results, we construct a continuum moiré Hamiltonian $\mathcal{H}$ for Dirac fermions in G/mXe based on symmetries (see the Appendix and Supplemental Material [33] for details). The form of $\mathcal{H}$ is similar to that of tBLG, but it couples Dirac fermions
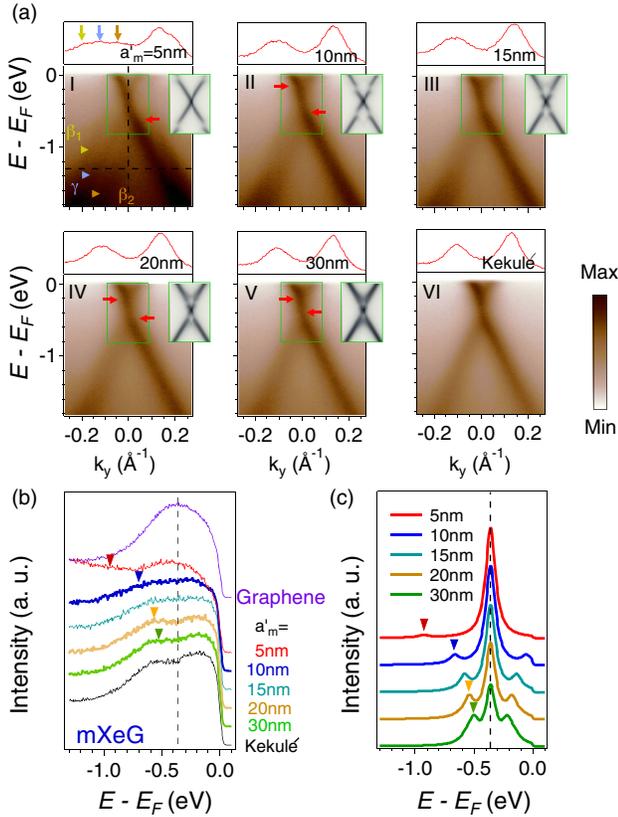
FIG. 4. (a) The band structure evolution near the K point, with different moiré period a'_m. The MDC at $E_B = 1.3$ eV are appended on top, with colored arrows indicating the β_1 and β_2 replicas and original γ cone. The simulated band structures for finite a'_m are appended with the same energy and k scales for a direct comparison. (b) The a'_m-dependent EDCs at the K point of G/mXe. The EDC of bare graphene is also plotted as purple line on the top. (c) The calculated EDCs at the K point of G/mXe for finite a'_m. Different curves are shifted vertically for clarity.

from two valleys in graphene, instead of from two layers in tBLG. The $\mathcal{H}$ captures the main features of the ARPES results, with replicas from two valleys located at the moiré BZ corners κ' and κ for a finite a'_m. We theoretically simulate the ARPES spectra near the K point. As shown in the insets of Fig. 4(a), hybridization gaps open at the crossing points between the γ cone and replicas, which is consistent with sudden intensity changes around the corresponding E_B marked by arrows. Similar to tBLG systems, the Dirac nodes remain gapless for a finite a'_m in our model because of $\hat{C}_{2z}\hat{T}$ symmetry, where $\hat{C}_{2z}$ is the twofold rotation symmetry around the z axis and $\hat{T}$ is time-reversal symmetry, and form a moiré band separated from other states. The bandwidth of this moiré band can be tuned by a'_m, and become nearly flat for large a'_m [Fig. 4(a-V) and Supplemental Material [33]].

Our model also describes the EDC evolution at the K point. As seen from Fig. 4(c), side peaks appears in the simulated EDC for $a'_m = 5$ nm, which correspond to the

spectra weight replicas at high E_B in ARPES results [Fig. 4(b)]. As a'_m increases, two side peaks corresponding to the upper and lower branches of replicas move close to the energy of the original γ Dirac node in the simulation. Because of the limitation of energy broadening in ARPES experiments, we observe a broader peak in EDC for $a'_m = 10$ nm, corresponding to three peaks close to each other in the model. Meanwhile, spectra weight transfers from the main peak of γ node to side peaks of replicas in the simulation. Therefore, we can experimentally resolve the two side peaks for $a'_m > 20$ nm. In the limit of $a'_m \to +\infty$ (i.e., $a_{Xe} = \sqrt{3}a_{Gra}$ and $\kappa \to 0$), the main peak at the Dirac point is expected to vanish and the two side peaks define the Kekulé gap $\Delta_{Kekulé}$. Because the experimental peak width is on the same order as $\Delta_{Kekulé}$, there are finite spectra weights inside $\Delta_{Kekulé}$ in ARPES results for $a'_m \to +\infty$. By using ARPES energy broadening, the simulated EDCs from the model can better reproduce the features of experimental results (Fig. S5 in the Supplemental Material [33]).

The large a'_m moiré pattern in G/mXe, in which flat moiré bands are predicted, can be realized in a wide range of temperatures. Above the second-layer desorption temperature T_s, a'_m can be tuned by Xe pressure P_{Xe} (Fig. S6 in the Supplemental Material [33]). Below T_s, a'_m can be tuned through different annealing processes (Fig. S7 in the Supplemental Material [33]).

In summary, we demonstrate an *in situ* tunable high-order moiré pattern in G/mXe with a'_m from nanometer scale to $+\infty$. The moiré pattern induced Dirac cone replicas are directly observed by ARPES measurements, which move in k space as a'_m changes in real space. The moiré pattern evolves into a Kekulé distortion at $a'_m \to +\infty$, and replicas overlap in k space with a gap opened at Dirac point. The theoretical model indicates flat band physics in G/mXe. We note that we use lab-based ARPES with 0.5 mm beam size in the current Letter. G/mXe provides an opportunity for ARPES probes of moiré physics without the need of nanoscale spatial resolution. Bands of both graphene and G/mXe observed here are broader than that of exfoliated graphene and tBLG [21,22], possibly due to the imperfection of graphene samples grown on SiC substrates. ARPES measurements on better quality graphene are helpful to resolve details of moiré bands for large a'_m. Transport measurements with gate tunable electron filling would provide smoking-gun evidence for the potential correlated states, superconductivity, and other flat band related quantum states in G/mXe. The high-order moiré pattern has also been observed in a graphene-SiC system [40], in which lattice mismatch Δa and twist angle θ are large between unit cells. We have realized graphene- and bilayer-graphene-based heterostructures consisting of other noble gas monolayers, e.g. krypton (Kr) and argon (Ar), and the *in situ* tunable high-order moiré pattern is generally observed. We also observed similar behaviors in

heterostructure consisting of layered vdW superconductor Cu_xTiSe_2 and monolayer Kr/Xe. Our Letter opens up vast new opportunities provided by the *in situ* tunable moiré patterns in designing quantum phases of 2D materials.

Appendix: Theoretical model.—The continuum moiré Hamiltonian $\mathcal{H}$ for the Dirac fermions in G/mXe is constructed based on symmetry analysis (See Supplemental Material [33]), and is given by

$$\mathcal{H} = \begin{pmatrix} h_+(\boldsymbol{k} - \boldsymbol{\kappa}_+) & T(\boldsymbol{r}) \\ T^\dagger(\boldsymbol{r}) & h_-(\boldsymbol{k} - \boldsymbol{\kappa}_-) \end{pmatrix}, \qquad \text{(A1)}$$

where the diagonal terms $h_\pm(\boldsymbol{k}) = \hbar v_F(\pm k_x \sigma_x + k_y \sigma_y)$ are the Dirac Hamiltonians for the two valleys, and $\sigma_{x,y}$ are Pauli matrices in the sublattice space. The momentum shifts $\boldsymbol{\kappa}_\pm = 4\pi/(3a'_m)(\mp 1/2, \sqrt{3}/2)$ connect the center and corners of the moiré BZ. The off-diagonal term $T(\boldsymbol{r})$ captures the intervalley coupling induced by the moiré superlattices, and is parametrized as follows:

$$T(\boldsymbol{r}) = T_0 + T_{+1}e^{i\boldsymbol{g}_2 \cdot \boldsymbol{r}} + T_{-1}e^{i\boldsymbol{g}_3 \cdot \boldsymbol{r}},$$
$$T_j = \begin{pmatrix} w_0 e^{-i2\pi j/3} & w_1 \\ w_1 & w_0 e^{i2\pi j/3} \end{pmatrix}, \qquad \text{(A2)}$$

where $\boldsymbol{g}_2 = 4\pi/(\sqrt{3}a'_m)(-\sqrt{3}/2, 1/2)$ and $\boldsymbol{g}_3 = 4\pi/(\sqrt{3}a'_m)(-\sqrt{3}/2, -1/2)$ are moiré reciprocal lattice vectors, and $w_{0,1}$ are two parameters.

In the limit of the moiré period $a'_m \to +\infty$, the vectors $\boldsymbol{\kappa}$, $\boldsymbol{\kappa}'$, and $\boldsymbol{g}_{2,3}$ all tend to vanish, and the moiré Hamiltonian $\mathcal{H}$ becomes

$$\mathcal{H}_{\text{Kekulé}} = \hbar v_F(k_x \tau_z \sigma_x + k_y \sigma_y) + 3w_1 \tau_x \sigma_x, \quad \text{(A3)}$$

where $\tau_{x,z}$ are Pauli matrices in the valley pseudospin space. The last term $3w_1 \tau_x \sigma_x$ in Eq. (A3) represents an intersublattice and intervalley coupling induced by Kekulé distortion, and gaps out the Dirac fermions with a gap given by $6w_1$. The experimentally measured Kekulé gap $\Delta_{\text{Kekulé}}$ is 0.4 eV. Therefore, we estimate that $w_1 = \Delta_{\text{Kekulé}}/6 \approx 67$ meV.

Terms in $T(\boldsymbol{r})$ that are proportional to w_0 correspond to on site potential modulations in the moiré superlattices, and break the particle-hole symmetry of the energy spectrum in the presence of a finite w_1. Because the ARPES measurement does not show significant particle-hole asymmetry for the Dirac cones, we take $w_0 = 0$ for simplicity in the calculation. Further studies are required to determine the values of $w_{0,1}$ from microscopic physics.

*These authors contributed equally to this work.
†Corresponding author.
nxu@whu.edu.cn
‡Corresponding author.
wufcheng@whu.edu.cn

[1] R. Bistritzer and A. H. MacDonald, Proc. Natl. Acad. Sci. U.S.A. **108**, 12233 (2011).

[2] Y. Cao, V. Fatemi, A. Demir, S. A. Fang, S. L. Tomarken, J. Y Luo, J. D. Sanchez-Yamagishi, K. Watanabe, T. Taniguchi, E. Kaxiras, R. C. Ashoori, and P. Jarillo-Herrero, Nature (London) **556**, 80 (2018).

[3] G. R. Chen, L. L. Jiang, S. Wu, B. Lyu, H. Y. Li, B. L. Chittari, K. Watanabe, T. Taniguchi, Z. W. Shi, J. Jung, Y. B. Zhang, and F. Wang, Nat. Phys. **15**, 237 (2019).

[4] G. W. Burg, J. H. Zhu, T. Taniguchi, K. Watanabe, A. H. MacDonald, and E. Tutuc, Phys. Rev. Lett. **123**, 197702 (2019).

[5] C. Shen, Y. B. Chu, Q. S. Wu, N. Li, S. P. Wang, Y. C. Zhao, J. Tang, J. Y. Liu, J. P. Tian, K. Watanabe, T. Taniguchi, R. Yang, Z. Y. Meng, D. X. Shi, O. V. Yazyev, and G. Y. Zhang, Nat. Phys. **16**, 520 (2020).

[6] Y. Cao, V. Fatemi, S. A. Fang, K. Watanabe, T. Taniguchi, E. Kaxiras, and P. Jarillo-Herrero, Nature (London) **556**, 43 (2018).

[7] X. B. Lu, P. Stepanov, W. Yang, M. Xie, M. A. Aamir, I. Das, C. Urgell, K. Watanabe, T. Taniguchi, G. Y. Zhang, A. Bachtold, A. H. MacDonald, and D. K. Efetov, Nature (London) **574**, 653 (2019).

[8] E. Codecido, Q. Y. Wang, R. Koester, S. Che, H. D. Tian, R. Lv, S. Tran, K. Watanabe, T. Taniguchi, F. Zhang, M. Bockrath, and C. N. Lau, Sci. Adv. **5**, eaaw9770 (2019).

[9] Y. Saito, J. Y. Ge, K. Watanabe, T. Taniguchi, and A. F Young, Nat. Phys. **16**, 926 (2020).

[10] P. Stepanov, I. Das, X. B. Lu, A. Fahimniya, K. Watanabe, T. Taniguchi, F. H. L. Koppens, J. Lischner, L. Levitov, and D. K. Efetov, Nature (London) **583**, 375 (2020).

[11] M. Yankowitz, S. W. Chen, H. Polshyn, Y. X. Zhang, K Watanabe, T. Taniguchi, D. Graf, A. F. Young, and C. R. Dean, Science **363**, 1059 (2019).

[12] H. S. Arora, R. Polski, Y. R. Zhang, A. Thomson, Y. Choi, H. Kim, Z. Lin, I. Z. Wilson, X. D. Xu, J. H. Chu, T. Watanabe, J. Alicea, and S. Nadj-Perge, Nature (London) **583**, 379 (2020).

[13] G. R. Chen, A. L. Sharpe, P. Gallagher, I. T. Rosen, E. J. Fox, L. L. Jiang, B. Lyu, H. Y. Li, K. Watanabe, T. Taniguchi, J. Jung, and Z. W. Shi, Nature (London) **572**, 215 (2019).

[14] A. L. Sharpe, E. J. Fox, A. W. Barnard, J. Finney, K. Watanabe, T. Takashi, M. A. Kastner, and G. Goldhaber-David, Science **365**, 605 (2019).

[15] Y. Cao, D. Rodan-Legrain, O. Rubies-Bigorda, J. M. Park, K. Watanabe, T. Taniguchi, and P. Jarillo-Herrero, Nature (London) **583**, 215 (2020).

[16] X. M. Liu, Z. Y. Hao, E. Khalaf, J. Y. Lee, Y. Ronen, H. Yoo, D. H. Najafabadi, K. Watanabe, T. Taniguchi, A. Vishwanath, and P. Kim, Nature (London) **583**, 221 (2020).

[17] M. H. He, Y. H. Li, J. Q. Cai, Y. Liu, T. Taniguchi, X. D. Xu, and M. Yankowitz, Nat. Phys. **17**, 26 (2021).

[18] M. Serlin, C. L. Tschirhart, H. Polshyn, Y. Zhang, J. Zhu, K. Watanabe, T. Taniguchi, L. Balents, and A. F. Young, Science **367**, 900 (2020).

[19] S. W. Chen, M. H. He, Y. H. Zhang, V. Hsieh, Z. Y. Fei, K. Watanabe, T. Taniguchi, D. H. Cobden, X. D. Xu, C. R. Dean, and M. Yankowitz, Nat. Phys. **17**, 374 (2021).

[20] G. R. Chen, A. L. Sharpe, E. J. Fox, Y. H. Zhang, S. X. Wang, L. L. Jiang, B. Lyu, H. Y. Li, K. Watanabe, T. Taniguchi, Z. W. Shi, T. Senthil, D. Goldhaber-Gordon, and Y. B. Zhang, Nature (London) **579**, 56 (2020).

[21] M. I. B. Utama, R. J. Koch, K. Lee, N. Leconte, H. Y. Li, S. H. Zhao, L. L. Jiang, J. Y. Zhu, K. Watanabe, T. Taniguchi, P. D. Ashby, A. Weber-Bargioni, A. Zettl, C. Jozwiak, J. Jung, E. Rotenberg, A. Bostwick, and F. Wang, Nat. Phys. **17**, 184 (2021).

[22] S. Lisi *et al.*, Nat. Phys. **17**, 189 (2021).

[23] F. C. Wu, T. Lovorn, E. Tutuc, and A. H. MacDonald, Phys. Rev. Lett. **121**, 026402 (2018).

[24] E. C. Regan, D. Q. Wang, C. H. Jin, M. I. B. Utama, B. N. Gao, X. Wei, S. H. Zhao, W. Y. Zhao, Z. C. Zhang, K. Yumigeta, M. Blei, J. D. Calstr'om, T. Watanabe, K. J. Taniguchi, S. Tongay, M. Crommie, A. Zettl, and F. Wang, Nature (London) **579**, 359 (2020).

[25] Y. H. Tang, L. Z. Li, T. X. Li, Y. Xu, S. Liu, K. Barmak, K. Watanabe, T. Taniguchi, A. H. MacDonald, J. Shan, and K. F. Mak, Nature (London) **579**, 353 (2020).

[26] Y. Xu, S. Liu, D. A. Rhodes, K. Watanabe, T. Taniguchi, J. Hone, V. Elser, K. F. Mak, and J. Shan, Nature (London) **587**, 214 (2020).

[27] L. Wang, E. M. Shih, A. Ghiotto, L. Xian, D. A. Rhodes, C. Tan, M. Claassen, D. M. Kennes, Y. S. Bai, B. Kim, K. Watanabe, Taniguchi, X. Y. Hone Zhou, A. J. Rubio, A. N. Pasupathy, and C. R. Dean, Nat. Mater. **19**, 861 (2020).

[28] H. Y. Li, S. W. Li, E. C. Regan, D. Q. Wang, W. Y. Zhao, S. Kahn, K. Yumigeta, M. Blei, T. Taniguchi, K. Watanabe, S. Tongay, A. Zettl, M. F. Crommie, and F. Wang, Nature (London) **597**, 650 (2021).

[29] R. Ribeiro-Palau, C. J. Zhang, K. Watanabe, T. Taniguchi, J. Hone, and C. R Dean, Science **361**, 690 (2018).

[30] N. R. Finney, M. Yankowitz, L. Muraleetharan, K. Watanabe, T. Taniguchi, C. R. Dean, and J. Hone, Nat. Nanotechnol. **14**, 1029 (2019).

[31] Q. Y. Wang, W. H. Zhang, L. L. Wang, K. He, X. C. Ma, and Q. K. Xue, J. Phys. Condens. Matter **25**, 095002 (2013).

[32] M. Hamichi, A. Q. D. Faisal, J. A. Venables, and R Kariotis, Phys. Rev. B **39**, 415 (1989).

[33] See Supplemental Material at http://link.aps.org/supplemental/10.1103/PhysRevLett.129.176402 for the moiré Brillouin zone of G/mXe, the valance band structure of Xe monolayer, LEED experiments with temperature cycling, the theory of moiré band structure of G/mXe, tuning high-order moiré pattern in G/mXe by Xe pressure and annealing process, which includes Refs. [34–37].

[34] K. Hermann, J. Noffke, and K. Horn, Phys. Rev. B **22**, 1022 (1980).

[35] T. Mandel, G. Kaindl, M. Demke, W. Fischer, and W. D. Schneider, Phys. Rev. Lett. **55**, 1638 (1985).

[36] M. Mucha-Kruczynski, O. Tsyplyatyev, A. Grishin, E. McCann, V. I. Falko, A. Bostwick, and E. Rotenberg, Phys. Rev. B **77**, 195403 (2008).

[37] Jihang Zhu, Jingtian Shi, and Allan H. MacDonald, Phys. Rev. B **103**, 235146 (2021).

[38] C. Y. Hou, C. Chamon, and C. Mudry, Phys. Rev. Lett. **98**, 186809 (2007).

[39] C. H. Bao, H. Y. Zhang, T. Zhang, X. Wu, L. P. Luo, S. H. Zhou, Q. Li, Y. H. Hou, W. Yao, L. W. Liu, P. Yu, J. Li, W. H. Duan, H. Yao, Y. L. Wang, and S. Y. Zhou, Phys. Rev. Lett. **126**, 206804 (2021).

[40] C. L. Wu, Q. Wan, C. Peng, S. K. Mo, R. Z. Li, K. M. Zhao, Y. P. Guo, D. Huo, C. D. Zhang, and N. Xu, Phys. Rev. B **104**, 235130 (2021).